

# Investigation of Stability and Magnetic Properties of Ni- and Co-Doped Iron Oxide Nano-particles

Safia Anjum<sup>1</sup> · Rabia Tufail<sup>1</sup> · Hafsa Saleem<sup>1</sup> · Rehana Zia<sup>1</sup> · Sira Riaz<sup>2</sup>

Received: 16 December 2016 / Accepted: 24 February 2017 / Published online: 10 March 2017  
© Springer Science+Business Media New York 2017

**Abstract** The current work is dedicated to investigate the effect of nickel and cobalt doping on the crystallinity, stability, and magnetic and optical properties of magnetite ( $\text{Fe}_3\text{O}_4$ ) nano-particles. Nickel- and cobalt-doped magnetite ( $\text{Ni}_x\text{Fe}_{3-x}\text{O}_4$  and  $\text{Co}_x\text{Fe}_{3-x}\text{O}_4$  with  $x = 0, 0.05, 0.1,$  and  $0.15$ ) nano-particles have been prepared by chemical co-precipitation method and are characterized by X-ray diffraction (XRD), Fourier transform infrared spectroscopy (FTIR), thermogravimetric analysis (DSC-TGA), scanning electron microscopy (SEM), vibrating sample magnetometry (VSM), and UV-visible spectroscopy to study their structural, thermal, morphological, magnetic, and optical properties, respectively. The structural analysis indicates the formation of a single-phase cubic inverse spinel structure with a decrease in lattice parameters with increasing Ni and Co concentrations. Thermal analysis reveals that the transition temperature increases. The increase in transition temperature is due to the maghemite to hematite phase transition after the replacement of  $\text{Fe}^{2+}$  with  $\text{Co}^{2+}$  or  $\text{Ni}^{2+}$  in the B-site. The increase in transition temperature is attributed to the fact that stability increases with increasing cobalt content. Morphological analysis indicates the spherical shape of nano-particles with least agglomeration at all

concentrations. The optical band gap energy increases as the particle size decreases. Magnetic properties reveal that the saturation magnetization decreases in both cases, but coercivity increases in the case of Co. This behavior is ascribed due to the high anisotropic cobalt cation doping in magnetite ( $\text{Fe}_3\text{O}_4$ ) nano-particles, which is the goal to achieve the increase in hyperthermic efficiency.

**Keywords** Nano-particles · Magnetic properties · Optical properties · Stability

## 1 Introduction

Magnetic nano-particles of the form  $\text{M}_x\text{Fe}_{3-x}\text{O}_4$  ( $\text{M} = \text{Ni}, \text{Co}, \text{Zn}, \text{Cr}, \text{etc.}$ ) have been an area of research during the recent years as they present many potential applications, such as catalysis [1, 2], targeted drug delivery [3], magnetic data storage [4], contrast agents for magnetic resonance imaging, and heat mediators in magnetic fluid hyperthermia [5–7]. These magnetic nano-particles are useful in order to enhance the biomedical applications because the properties of nano-particles remarkably changed from their bulk counterpart. One of the most interesting properties of magnetic nano-particles is the ability to generate heat under the influence of alternating magnetic field. The heating effect can be obtained from the magnetic hysteresis losses that occur during the magnetization reversal process [8]. Among various magnetic nano-particles, magnetite and cation-substituted magnetite (such as Ni and Co) nano-particles are useful candidates for this purpose. Both of these transition metals can significantly increase the hyperthermic efficiency through a partial or total substitution of high anisotropic  $\text{Ni}^{2+}$  or  $\text{Co}^{2+}$  ions with  $\text{Fe}^{2+}$  ions in the magnetite structure [9].

✉ Safia Anjum  
safia\_anjum@hotmail.com

<sup>1</sup> Department of Physics, Lahore College for Women University, Lahore, Pakistan

<sup>2</sup> Center of Excellence in Solid State Physics, University of the Punjab, Lahore, Pakistan

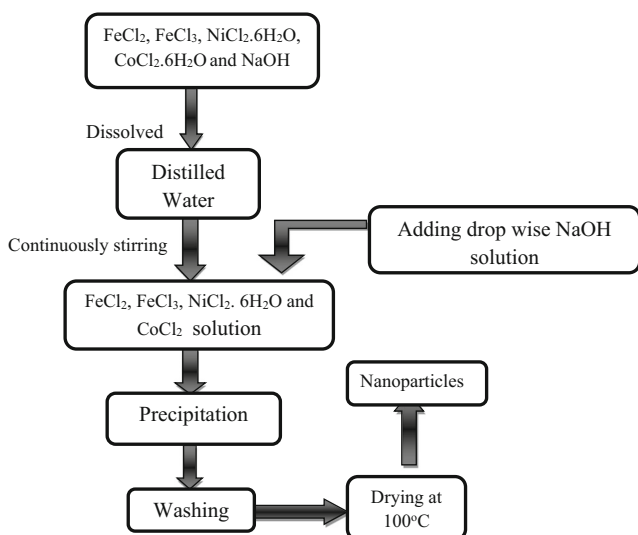


**Fig. 1** Block diagram of co-precipitation method

Magnetite has the inverse spinel cubic structure represented as



It has 8  $\text{Fe}^{2+}$  ions at the octahedral site, and 32 oxygen ions and 16  $\text{Fe}^{3+}$  ions are equally distributed among the tetrahedral and octahedral sites [10]. Magnetism of magnetite is the result of super-exchange interactions between tetrahedral and octahedral cations which result in anti-parallel magnetic moments between them. In the magnetite structure, net magnetization is exhibited by the  $\text{Fe}^{2+}$  ions [11]. In the cation-substituted magnetite nano-particles, the divalent ions are replaced by  $\text{Fe}^{2+}$  ions which can significantly change their magnetic properties [12]. The nickel- and cobalt-doped magnetite nano-particles also have an inverse spinel cubic structure in which metal ions occupy octahedral site and ferric ions are equally distributed among the tetrahedral and octahedral sites.

A variety of methods have been used for the synthesis of magnetic nano-particles such as sol-gel method [13], co-precipitation [14–16], and hydrothermal [17] and thermal

decomposition [18, 19]. Among these, the co-precipitation method is mostly used for preparation of MNPs because it is the simplest and cheapest method [20] and no further heat treatment is required to achieve a structure. In this work,  $\text{Ni}_x\text{Fe}_{3-x}\text{O}_4$  and  $\text{Co}_x\text{Fe}_{3-x}\text{O}_4$  with  $x = 0, 0.05, 0.1,$  and  $0.15$  nano-particles are prepared using the co-precipitation method in order to investigate the effect of Ni and Co doping on structural, thermal, morphological, magnetic, and optical properties of magnetite nano-particles.

## 2 Experimental Method

### 2.1 Synthesis of $\text{Ni}_x\text{Fe}_{3-x}\text{O}_4$ and $\text{Co}_x\text{Fe}_{3-x}\text{O}_4$ Nano-particles

The  $\text{Ni}_x\text{Fe}_{3-x}\text{O}_4$  and  $\text{Co}_x\text{Fe}_{3-x}\text{O}_4$  nano-particles with  $x = 0, 0.05, 0.1,$  and  $0.15$  have been prepared using the co-precipitation method; the block diagram is shown in Fig. 1. Chloride salts ( $\text{FeCl}_2, \text{FeCl}_3, \text{CoCl}_2,$  and  $\text{NiCl}_2$ ) are used as starting materials. Each salt is dissolved in double-distilled water separately. In the present case, 0.05 M solution of both cobalt and nickel is used in 0.01 and 1.7 M solution of ferrous and ferric chlorides, respectively. Then the previous solution was added to each other, and sodium hydroxide solution (3 M) was added drop wise in this solution. The precipitates were washed with double-distilled water and ethanol several times. The precipitation was dried in an oven at  $80^\circ\text{C}$  for several hours.

### 2.2 Characterization Techniques

The crystal structures and phase composition of the samples are studied using Philips X-ray diffraction (XRD) with  $\text{CuK}\alpha$  radiation ( $\lambda = 1.5418 \text{ \AA}$ ) at a scanning rate of  $2^\circ/\text{min}$  in the scanning range of  $30\text{--}140^\circ$ . The functional groups are analyzed by Perkin Elmer FTIR spectrometer. To investigate the thermal stability of prepared nano-particles, thermogravimetric analysis (TGA) and differential scanning calorimetric (DSC) studies have been carried out. This

**Fig. 2** XRD patterns of all the samples of **a**  $\text{Ni}_x\text{Fe}_{3-x}\text{O}_4$  and **b**  $\text{Co}_x\text{Fe}_{3-x}\text{O}_4$  nano-particles

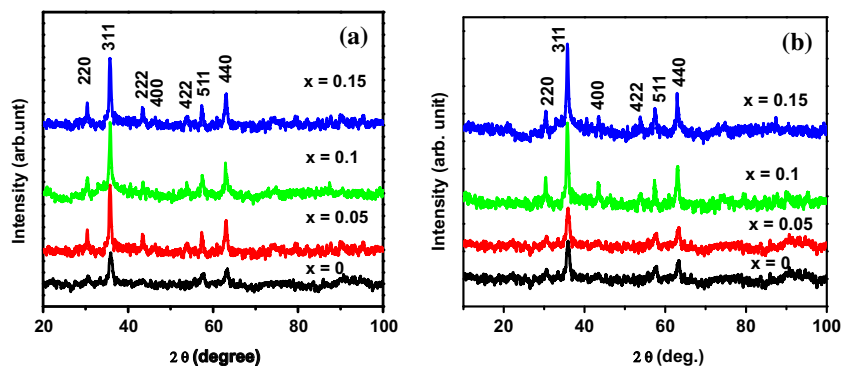


**Table 1** XRD data of  $Ni_xFe_{3-x}O_4$  and  $Co_xFe_{3-x}O_4$  nano-particles

Composition ( $x$ )	Position ( $2\theta$ )	FWHM (deg)	d-spacing (Å)	Crystallite size (nm)	Lattice parameters (Å)	X-ray density (g/cm <sup>3</sup> )
$Fe_3O_4$	35.927	0.76859	2.4976	10.3	8.3910	5.3641
$Ni_{0.05}Fe_{2.95}O_4$	35.761	0.84357	2.5089	9.2	8.3608	5.2066
$Ni_{0.10}Fe_{2.9}O_4$	35.788	0.89509	2.5070	8.5	8.3607	5.2098
$Ni_{0.15}Fe_{2.85}O_4$	35.764	0.91297	2.5086	7.6	8.3536	5.2130
$Co_{0.05}Fe_{2.95}O_4$	35.735	0.85231	2.5161	9.7	8.3901	5.3217
$Co_{0.1}Fe_{2.9}O_4$	35.781	0.89459	2.5153	7.2	8.3893	5.3421
$Co_{0.15}Fe_{2.85}O_4$	35.809	0.89782	2.5181	6.5	8.3882	5.2213

analysis is done with TGA/DSC (Mettler Toledo Ltd.) instrument at a heating rate of 10 °C/min at room temperature to 1000 °C in nitrogen atmosphere. UV-visible spectra are recorded using a Perkin Elmer Lambda spectrophotometer. SEM are carried out using a Philips Morgagni Scanning Electron Microscope. The magnetic properties of samples are characterized with an Oxford Lake Shore’s Vibrating Sample Magnetometer (VSM) using an applied field of 10 kOe.

### 3 Results and Discussion

#### 3.1 Structural Analysis

The XRD pattern of the  $Ni_xFe_{3-x}O_4$  and  $Co_xFe_{3-x}O_4$  where  $x = 0, 0.05, 0.1,$  and  $0.15$  nano-particles is shown in Fig. 2. All the peaks are indexed with JPCD card no.19-0629 which corresponds to an inverse spinel structure of nano-particles. The strong peaks suggested that  $Ni_xFe_{3-x}O_4$  and  $Co_xFe_{3-x}O_4$  nano-particles are highly crystalline. The crystallinity increases with nickel and cobalt doping in magnetite nano-particles. The broadening in the peaks indicates that the particle size is at nano-domain. All XRD patterns show diffraction peaks which correspond to the spinel phase of  $Ni_xFe_{3-x}O_4$  and  $Co_xFe_{3-x}O_4$  nano-particles. The parameters extracted from the XRD micrographs are tabulated in Table 1.

The crystallite size of nano-particles is calculated from the FWHM of (311) diffraction peaks using Debye-Scherrer formula [21]:

$$D_p = \frac{0.94\lambda}{\beta \cos\theta} \tag{2}$$

where  $\beta$  is the full width at half maximum,  $\lambda$  shows the wavelength of  $CuK\alpha$  ( $\lambda = 1.54 \text{ \AA}$ ), and  $\theta$  is the Bragg angle. It is observed that particle size decreases with nickel and cobalt doping in magnetite nano-particles which is due to the broadening of the diffracted peaks.

The lattice parameter calculated from the formula [22]:

$$a = (d(h^2 + k^2 + l^2)^{1/2}) \tag{3}$$

where  $h, k,$  and  $l$  are the miller indices. The lattice parameters decrease with increasing nickel and cobalt concentrations, as shown in Fig. 3. This is due to the small ionic radii of Ni (0.69 Å) and Co (0.74 Å) as compared with the ionic radii of  $Fe^{2+}$  (0.77 Å). The X-ray density is calculated using the formula [23]:

$$d_x = \frac{8M}{Na^3} \tag{4}$$

where  $M$  is the molecular weight and  $N$  is the Avogadro number ( $6.02214 \times 10^{23}$ ). The lattice parameters increase with increasing concentration of nickel and cobalt, which is due to the greater molecular weight of nickel

**Fig. 3** Variation of crystallite size and lattice parameters of **a**  $Ni_xFe_{3-x}O_4$  and **b**  $Co_xFe_{3-x}O_4$  nano-particles

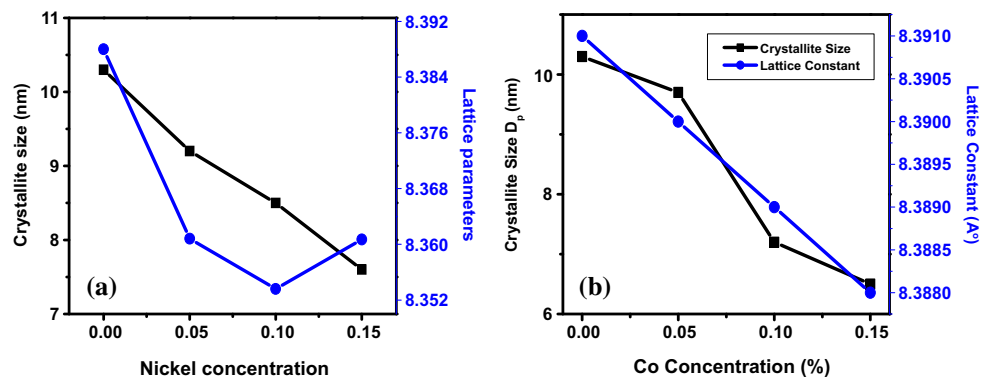
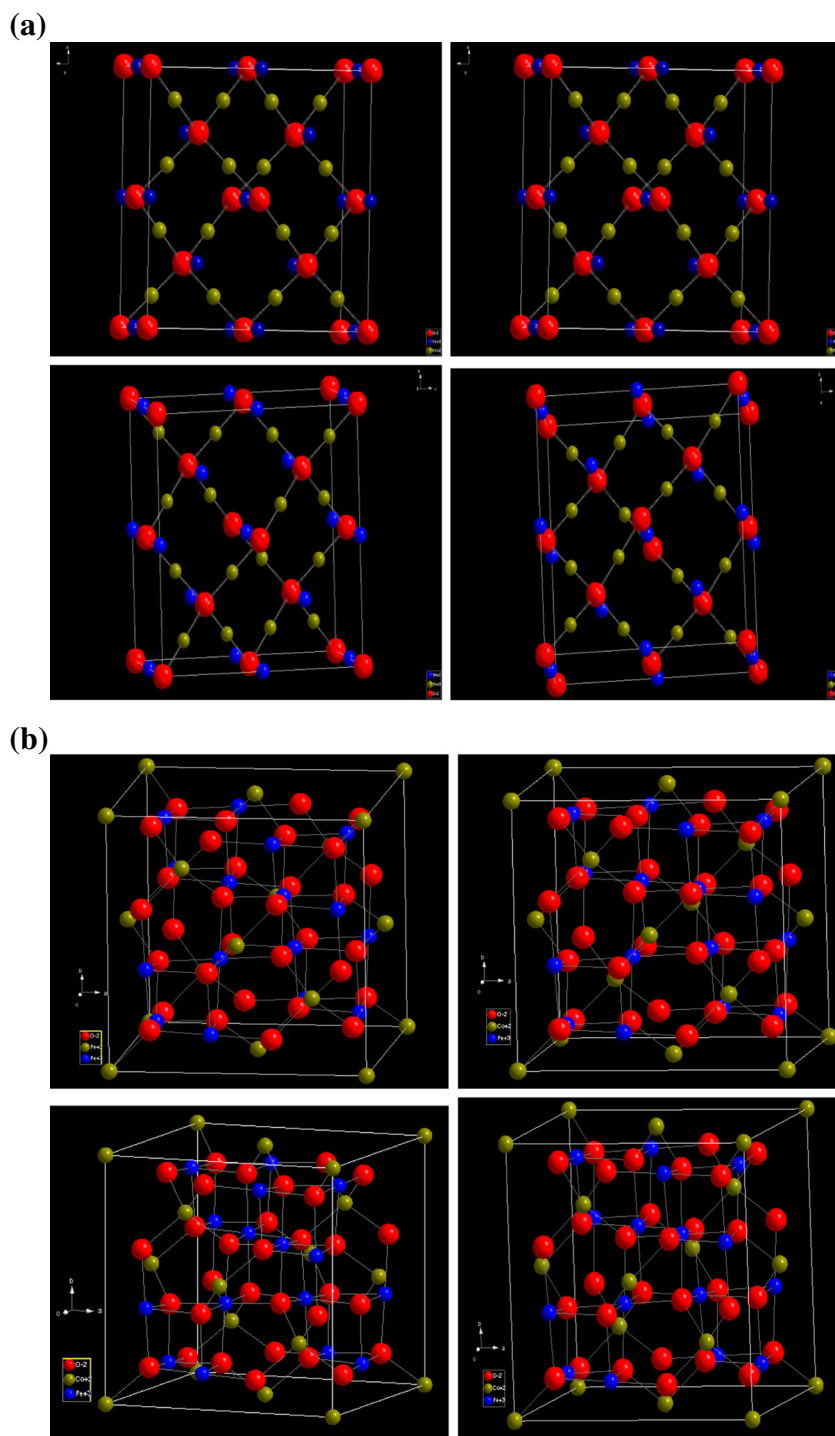


**Fig. 4** **a** 3-D structure of  $\text{Ni}_x\text{Fe}_{3-x}\text{O}_4$  with  $x = 0, 0.05, 0.1,$  and  $0.15$  nano-particles. **b** 3-D structure of  $\text{Co}_x\text{Fe}_{3-x}\text{O}_4$  with  $x = 0, 0.05, 0.1,$  and  $0.15$  nano-particles



(58.6934 g/mol) and cobalt (58.9331 g/mol) as compared with Fe (55.845 g/mol).

### 3.1.1 Diamond Structure

The 3-D structural view of  $\text{Ni}_x\text{Fe}_{3-x}\text{O}_4$  and  $\text{Co}_x\text{Fe}_{3-x}\text{O}_4$  nano-particles is shown in Fig. 4a, b, respectively. The Wyckoff sites and  $x$ ,  $y$ , and  $z$  values for all the elements

used are listed in Table 2, and parameters obtained from this software are listed in Table 3. The cell volume values are confirmed with the help of the Diamond software using  $V = a^3$ . It is evident from the micrographs that there is a slight difference in these structures because of the small variations in the lattice parameters. It is observed from Table 1 that lattice parameter  $a$  decreases with increasing nickel and cobalt content, and, therefore, the unit cell volume is

**Table 2** Atomic coordinates of Ni<sub>x</sub>Fe<sub>3-x</sub>O<sub>4</sub> and Co<sub>x</sub>Fe<sub>3-x</sub>O<sub>4</sub> (x = 0, 0.05, 0.1, and 0.15) nano-particles

Atom	Ox.	Wyck.	X	y	z
Fe	+2	16c	1/8	1/8	1/8
Fe	+3	8b	5/8	5/8	5/8
O	-2	32e	0.38672	0.38672	0.38672
Ni	+2	8b	1/2	1/2	1/2
Co	+2	8a	0	0	0

small for the highest Ni and Co concentrations, as shown in Fig. 4a, b.

### 3.2 FTIR Analysis

In order to characterize the as-synthesized nano-particles, FTIR spectroscopy was performed in the wavelength range 600–4000 cm<sup>-1</sup>. The FTIR spectra of Co<sub>x</sub>Fe<sub>3-x</sub>O<sub>4</sub> and Ni<sub>x</sub>Fe<sub>3-x</sub>O<sub>4</sub> (x = 0, 0.05, 0.1, and 0.15) nano-particles are shown in Fig. 5a, b, respectively. The obtained spectra are mainly characterized by the presence of organic compounds remaining from the co-precipitation synthesis procedure. The band at 2909.82 cm<sup>-1</sup> is attributed to the vibration mode of the O–H bond in the water molecule that remained absorbed in the nano-particle surface during synthesis. The bands at 2359 cm<sup>-1</sup> is ascribed to the C–H bond. The band at 1600 cm<sup>-1</sup> to 1102 cm<sup>-1</sup> are due to the C=O and C–O bonds. The two M–O bonds in the range of 780–890 cm<sup>-1</sup> confirms the formation of inverse spinel structure of both types of nano-particles.

### 3.3 DSC/TGA Analysis

The thermal characterization of Ni<sub>x</sub>Fe<sub>3-x</sub>O<sub>4</sub> and Co<sub>x</sub>Fe<sub>3-x</sub>O<sub>4</sub> nano-particles with x = 0, 0.05, 0.1, and 0.15 are performed by DSC/TGA analysis. The experiments were carried out in nitrogen atmosphere. The TGA curve of Ni<sub>x</sub>Fe<sub>3-x</sub>O<sub>4</sub> and Co<sub>x</sub>Fe<sub>3-x</sub>O<sub>4</sub> nano-particles is shown in Fig. 6a, b, respectively. As the temperature increases from

**Table 3** Cell volume and density values for Ni<sub>x</sub>Fe<sub>3-x</sub>O<sub>4</sub> and Co<sub>x</sub>Fe<sub>3-x</sub>O<sub>4</sub> with x = 0, 0.05, 0.1, and 0.15 nano-particles

Sample	Cell volume (Å <sup>3</sup> )	Density (g/cm <sup>3</sup> )
Fe <sub>3</sub> O <sub>4</sub>	590.55	5.211
Ni <sub>0.05</sub> Fe <sub>2.95</sub> O <sub>4</sub>	590.45	5.288
Ni <sub>0.10</sub> Fe <sub>2.9</sub> O <sub>4</sub>	590.28	5.290
Ni <sub>0.15</sub> Fe <sub>2.85</sub> O <sub>4</sub>	590.12	5.295
Co <sub>0.05</sub> Fe <sub>2.95</sub> O <sub>4</sub>	590.50	5.277
Co <sub>0.1</sub> Fe <sub>2.9</sub> O <sub>4</sub>	590.38	5.281
Co <sub>0.15</sub> Fe <sub>2.85</sub> O <sub>4</sub>	590.17	5.299

30 to 150 °C, 2.5% weight loss is observed in both nickel- and cobalt-doped magnetite nano-particles. This is due to the moisture which is absorbed during the experiment.

The DCS graphs of as-synthesized Ni<sub>x</sub>Fe<sub>3-x</sub>O<sub>4</sub> and Co<sub>x</sub>Fe<sub>3-x</sub>O<sub>4</sub> nano-particles with x = 0, 0.05, 0.1, and 0.15 nano-particles is shown in Fig. 7a, b, respectively. The graphs shows the variation of heat flow as a function of temperature. The change in enthalpy is calculated by using the formula [24]:

$$\Delta H = \frac{Q_2 - Q_1}{T_2 - T_1} \tag{5}$$

First, calculate Q<sub>2</sub>–Q<sub>1</sub> from y-axis and then T<sub>2</sub>–T<sub>1</sub> from x-axis and then divide both values. The values of enthalpy change of Ni<sub>x</sub>Fe<sub>3-x</sub>O<sub>4</sub> and Co<sub>x</sub>Fe<sub>3-x</sub>O<sub>4</sub> nano-particles with x = 0, 0.05, 0.1, and 0.15 nano-particles with increasing transition temperature is shown in Table 3. A sharp exothermic peak was observed in magnetite nano-particles at ~336 °C temperature due to the phase transition from γ-Fe<sub>2</sub>O<sub>3</sub> to α-Fe<sub>2</sub>O<sub>3</sub> [25]. The peak starts at T<sub>1</sub> (207 °C) and ends at T<sub>2</sub> (339 °C) with an enthalpy change of –6.8 J/g. When the concentration of nickel and cobalt is increased, the value of enthalpy decreases and is listed in Table 4. The variation of enthalpy change and transition temperature as a function of the cobalt and nickel concentrations is shown on Fig. 8a, b, respectively. It is observed that when the concentration of nickel increases, the transition temperature increases and enthalpy decreases.

### 3.4 SEM Analysis

The surface topography and morphology of Ni<sub>x</sub>Fe<sub>3-x</sub>O<sub>4</sub> and Co<sub>x</sub>Fe<sub>3-x</sub>O<sub>4</sub> nano-particles with x = 0, 0.05, 0.1, and 0.15 nano-particles are shown in Figs. 9a–d and 10a–d, respectively. The SEM specimens are prepared by dispersing the powdered compounds in deionized water and sonicating them for 30 min [26]. One drop of the sonicated solution is placed on the silicon wafer and then dried with the help of a hot plate. The figures indicate that the shape of both nickel- and cobalt-doped magnetite nano-particles are spherical with little agglomeration.

### 3.5 Magnetic Properties

The hysteresis loops for Ni<sub>x</sub>Fe<sub>3-x</sub>O<sub>4</sub> and Co<sub>x</sub>Fe<sub>3-x</sub>O<sub>4</sub> nano-particles with x = 0, 0.05, 0.1, and 0.15 are shown in Fig. 11a, b, respectively. The values of coercivity (H<sub>c</sub>), saturation magnetization (M<sub>s</sub>), remanence (M<sub>r</sub>), anisotropy, and magnetic moment are tabulated in Table 5. It is observed that the value of magnetization is decreased with increasing nickel and cobalt concentrations, because Ni<sup>2+</sup> and Co<sup>2+</sup> ions replace the Fe<sup>2+</sup> ions on the octahedral sites. The magnetic moment of Ni<sup>2+</sup> (2μ<sub>B</sub>) Co<sup>2+</sup> (3μ<sub>B</sub>) [27] is less

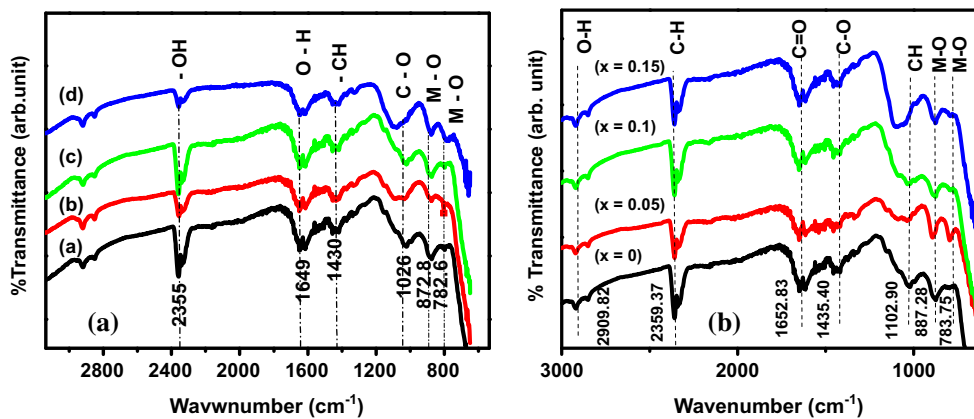


**Fig. 5** FTIR micrographs of **a**  $\text{Ni}_x\text{Fe}_{3-x}\text{O}_4$  and **b**  $\text{Co}_x\text{Fe}_{3-x}\text{O}_4$  nano-particles

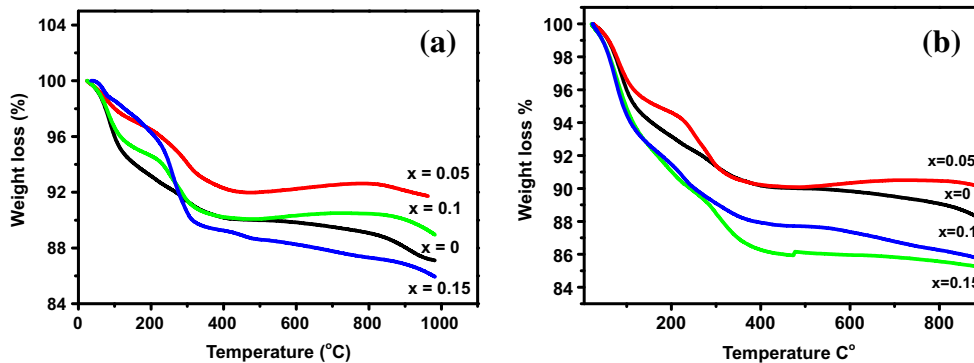


**Fig. 6** Variation in percent weight loss as a function of temperature (TGA curve) for **a**  $\text{Ni}_x\text{Fe}_{3-x}\text{O}_4$  and **b**  $\text{Co}_x\text{Fe}_{3-x}\text{O}_4$  nano-particles

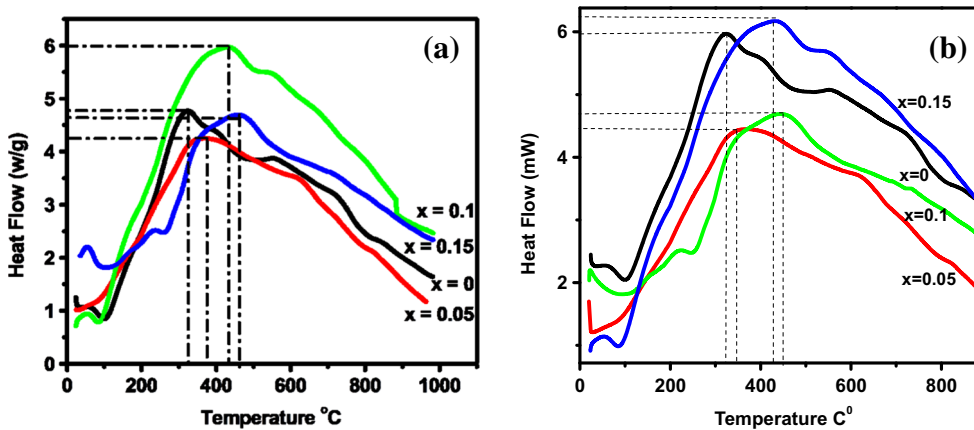
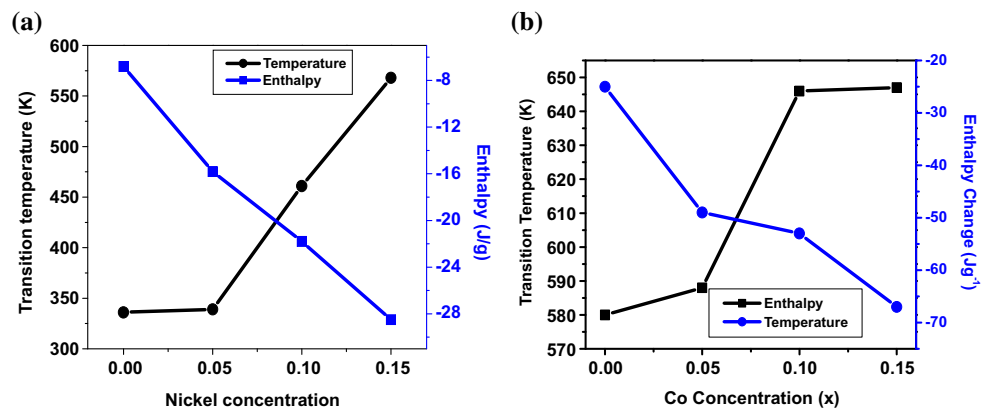


**Fig. 7** Variation in heat flow as a function of temperature (DSC curve) for **a**  $\text{Ni}_x\text{Fe}_{3-x}\text{O}_4$  and **b**  $\text{Co}_x\text{Fe}_{3-x}\text{O}_4$  nano-particles

**Table 4** Values of enthalpy and phase transition temperature of **a**  $\text{Ni}_x\text{Fe}_{3-x}\text{O}_4$  and **b**  $\text{Co}_x\text{Fe}_{3-x}\text{O}_4$  nano-particles

Samples	Transition temperature (°C)	Enthalpy change ( $\text{J g}^{-1}$ )
$\text{Fe}_3\text{O}_4$	580	-6.80
$\text{Ni}_{0.05}\text{Fe}_{2.95}\text{O}_4$	339	-15.8
$\text{Ni}_{0.1}\text{Fe}_{2.9}\text{O}_4$	461	-21.8
$\text{Ni}_{0.15}\text{Fe}_{2.85}\text{O}_4$	568	-28.5
$\text{Co}_{0.05}\text{Fe}_{2.95}\text{O}_4$	588	-49
$\text{Co}_{0.1}\text{Fe}_{2.9}\text{O}_4$	646	-53
$\text{Co}_{0.15}\text{Fe}_{2.85}\text{O}_4$	647	-67

**Fig. 8** Variation in enthalpy and transition temperature of **a**  $\text{Ni}_x\text{Fe}_{3-x}\text{O}_4$  and **b**  $\text{Co}_x\text{Fe}_{3-x}\text{O}_4$  nano-particles as a function of cobalt and nickel concentrations



than that of  $\text{Fe}^{2+}$  ( $4\mu_B$ ). This is in accordance with the Neel's sublattice model; firstly,  $\text{Ni}^{2+}$  and  $\text{Co}^{2+}$  ions cause the shifting of  $\text{Fe}^{3+}$  ions from tetrahedral to octahedral site, but when the concentration of nickel and cobalt ions increases, the tetrahedral-octahedral interactions decrease and the octahedral-octahedral interactions increase. As a result, the total magnetic moment of the system is decreased and therefore magnetization also decreased.

It is also revealed that the coercivity increases with increasing quantity of nickel and cobalt substitution. This

is because of the decrease in crystallite size by the doping of nickel and cobalt ions. As the crystallite size decreases, the number of domain walls decreases and the chances of magnetization and demagnetization of a material decreases. The anisotropy constant  $K$  is calculated using the following the relation [28].

$$K = \frac{M_s \times H_c}{0.98} \tag{6}$$

**Fig. 9** SEM micrographs of **a**  $\text{Fe}_3\text{O}_4$ , **b**  $\text{Co}_{0.05}\text{Fe}_{2.95}\text{O}_4$ , **c**  $\text{Co}_{0.05}\text{Fe}_{2.9}\text{O}_4$ , and **d**  $\text{Co}_{0.05}\text{Fe}_{2.85}\text{O}_4$  nano-particles at  $50\ \mu\text{m}$  resolution

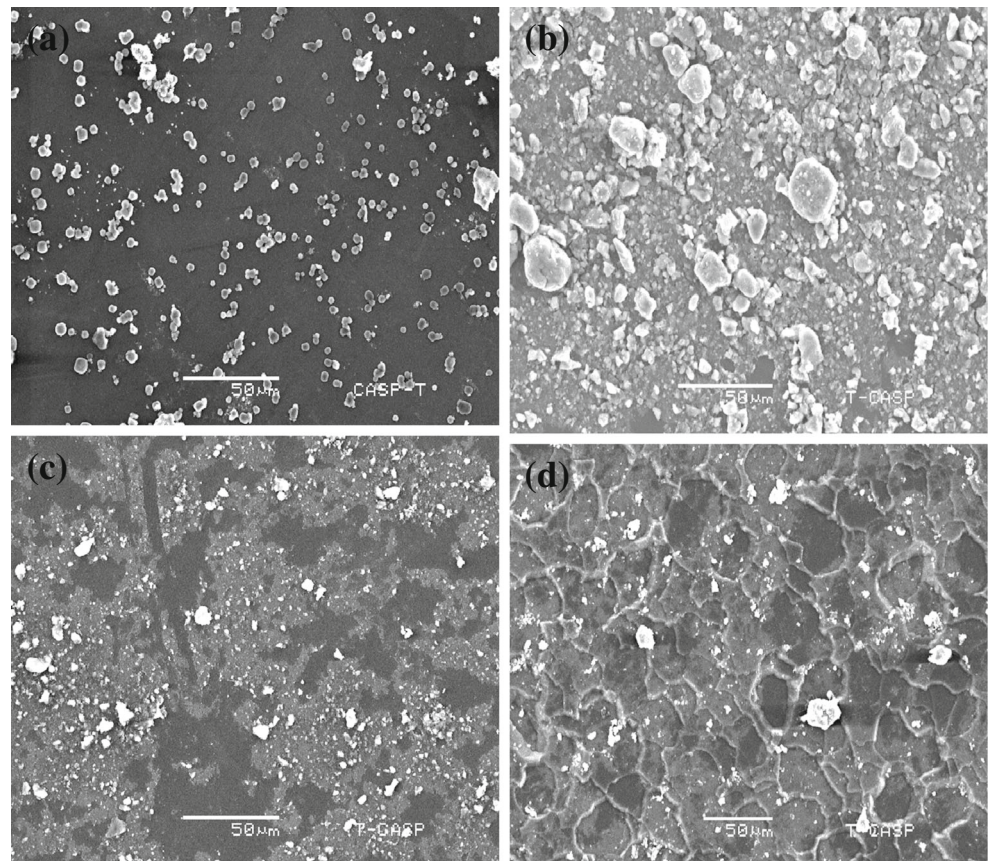
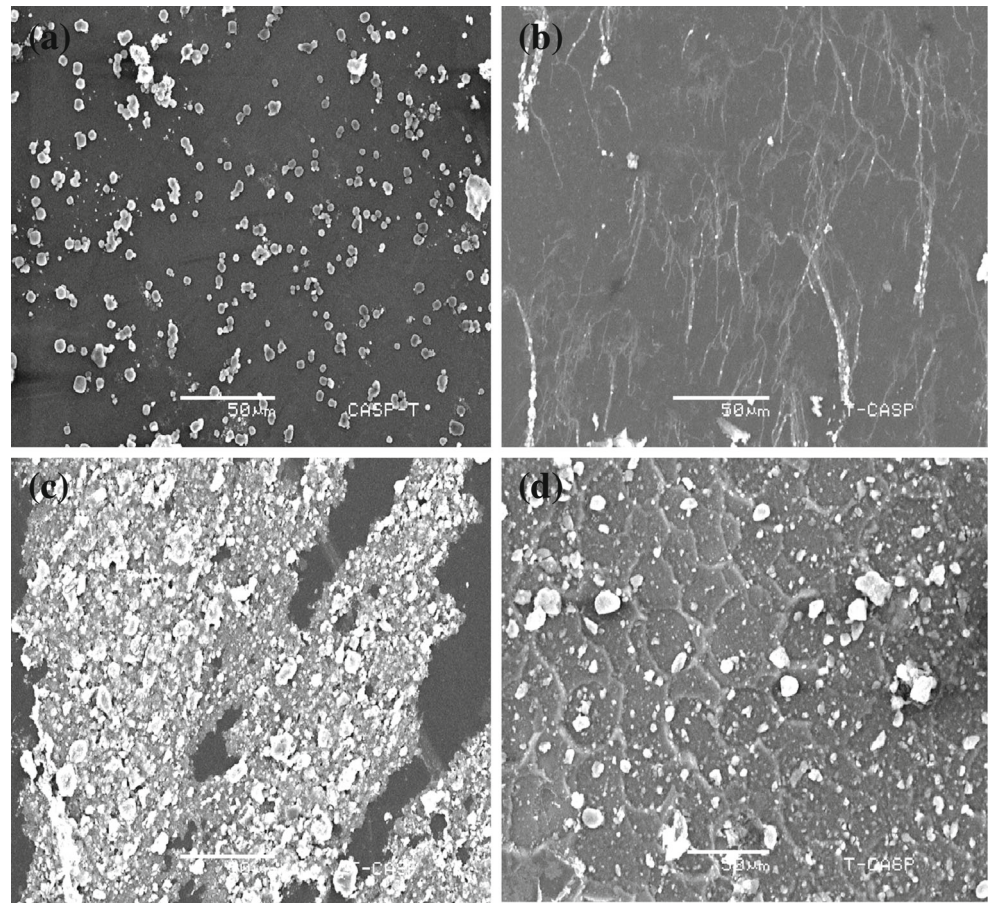


**Fig. 10** SEM micrographs of **a**  $\text{Fe}_3\text{O}_4$ , **b**  $\text{Ni}_{0.05}\text{Fe}_{2.95}\text{O}_4$ , **c**  $\text{Ni}_{0.05}\text{Fe}_{2.9}\text{O}_4$ , and **d**  $\text{Ni}_{0.05}\text{Fe}_{2.85}\text{O}_4$  nano-particles at  $50\ \mu\text{m}$  resolution



where  $H_c$  and  $M_s$  are the coercivity and saturation magnetization, respectively. Anisotropy constant  $K$  depends on the substituted ion concentration. This means that the anisotropy constant increases with increasing nickel content and therefore the magnitude of  $H_c$  also increases. This effect appears largest for the highest cobalt-concentrated sample that shows a highest value of coercivity.

The magnetic moment ( $n_B$ ) is calculated from the following formula [29]:

$$n_B = \frac{M \times M_s}{5588} \quad (7)$$

where  $M$  is molecular weight. The values of magnetic moments show that all the samples are ferromagnetic in nature.

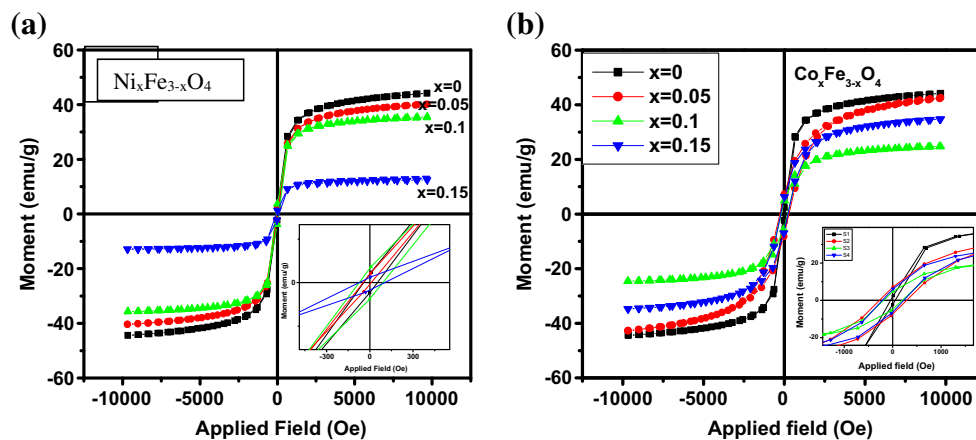


**Fig. 11** Hysteresis loops of **a**  $\text{Ni}_x\text{Fe}_{3-x}\text{O}_4$  and **b**  $\text{Co}_x\text{Fe}_{3-x}\text{O}_4$  ( $x = 0, 0.05, 0.1,$  and  $0.15$ ) nano-particles



**Table 5** Magnetic properties of  $Ni_xFe_{3-x}O_4$  and  $Co_xFe_{3-x}O_4$  nano-particles

Samples	Magnetization ( $M_s$ (emu/g))	Coercivity ( $H_c$ (Oe))	Remanance ( $M_r$ (emu/g))	Magnetic moment ( $n_B$ )	Anisotropy ( $K$ (erg/g))
$Fe_3O_4$	45.50	54.08	2.077	1.47	1969
$Ni_{0.05}Fe_{2.95}O_4$	44.33	78.26	3.471	1.29	2495
$Ni_{0.10}Fe_{2.9}O_4$	32.25	97.42	4.897	1.31	3151
$Ni_{0.15}Fe_{2.85}O_4$	9.14	99.31	4.574	0.44	3380
$Co_{0.05}Fe_{2.95}O_4$	42.4	183.20	4.41	1.41	1882
$Co_{0.1}Fe_{2.9}O_4$	25.3	181.22	4.7	0.80	3689
$Co_{0.15}Fe_{2.85}O_4$	35.9	184.86	4.85	0.77	3788

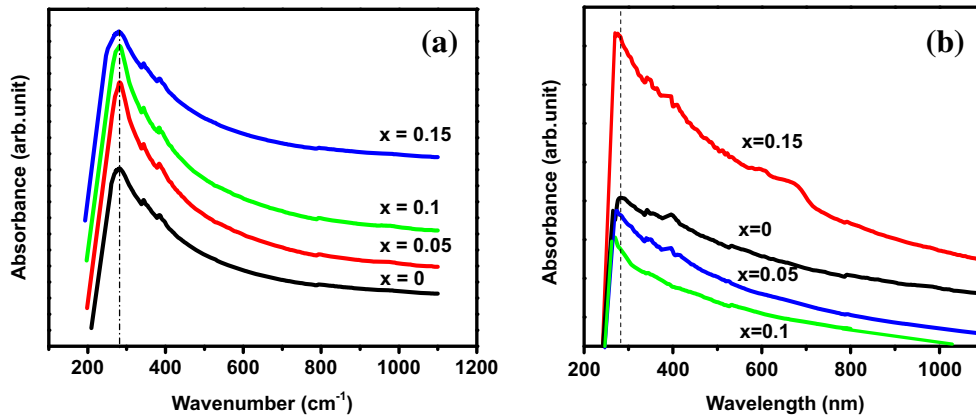


**Fig. 12** UV-Vis absorption spectra for **a**  $Ni_xFe_{3-x}O_4$  and **b**  $Co_xFe_{3-x}O_4$  nano-particles

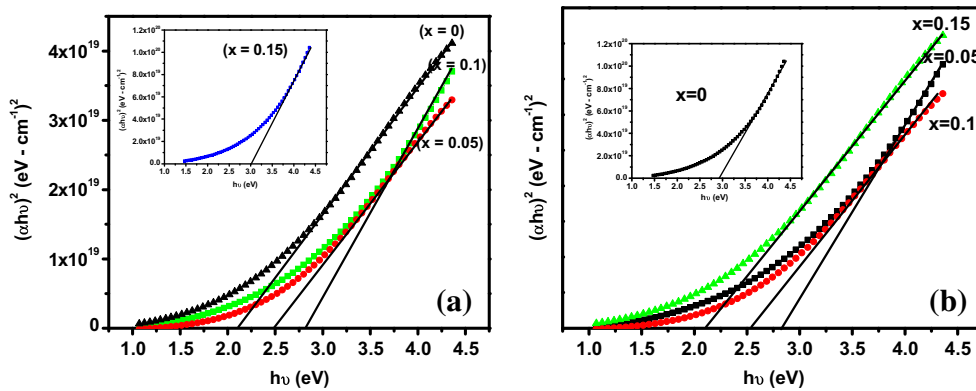


**Fig. 13** Determination of optical band gap for **a**  $Ni_xFe_{3-x}O_4$  and **b**  $Co_xFe_{3-x}O_4$

**Fig. 14** Variation in band gap energy and crystallite size as a function of **a** nickel and **b** cobalt concentrations

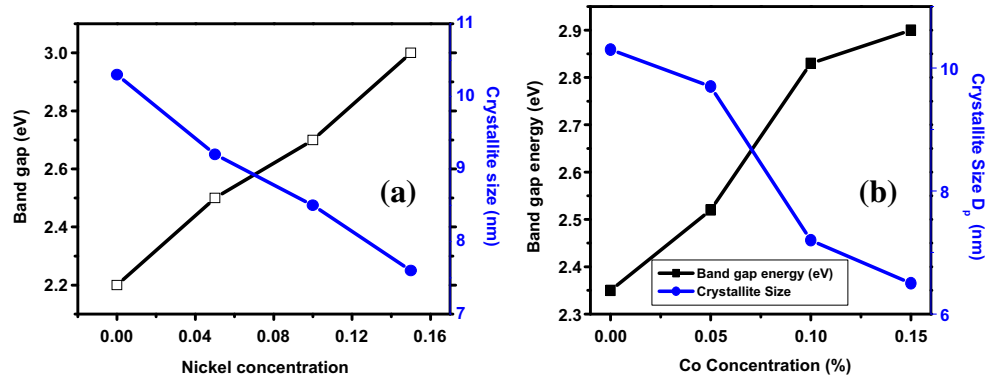


**Table 6** The absorption wavelength, band gap energy, and crystallite size values for  $\text{Ni}_x\text{Fe}_{3-x}\text{O}_4$  and  $\text{Co}_x\text{Fe}_{3-x}\text{O}_4$  with  $x = 0, 0.05, 0.1,$  and  $0.15$  nano-particles

Samples	Absorption $\lambda$ (nm)	Direct band gap energy(eV)	Crystallite size (nm)
$\text{Fe}_3\text{O}_4$	284	2.35	10.3
$\text{Ni}_{0.05}\text{Fe}_{2.95}\text{O}_4$	281	2.5	9.2
$\text{Ni}_{0.1}\text{Fe}_{2.9}\text{O}_4$	279	2.7	8.5
$\text{Ni}_{0.15}\text{Fe}_{2.85}\text{O}_4$	276	3.0	7.6
$\text{Co}_{0.05}\text{Fe}_{2.95}\text{O}_4$	279	2.52	9.7
$\text{Co}_{0.1}\text{Fe}_{2.9}\text{O}_4$	272	2.83	7.2
$\text{Co}_{0.15}\text{Fe}_{2.85}\text{O}_4$	269	2.90	6.5

### 3.6 Optical Properties

The optical properties of  $\text{Ni}_x\text{Fe}_{3-x}\text{O}_4$  and  $\text{Co}_x\text{Fe}_{3-x}\text{O}_4$  with  $x = 0, 0.05, 0.1,$  and  $0.15$  are determined using UV-visible spectroscopy. For this purpose, the samples are prepared by dissolving each sample in 10 ml of DMF solution. Figure 12a, b shows the absorbance versus wavelength curves of all the samples. The shifting in wavelength for  $\text{Ni}_x\text{Fe}_{3-x}\text{O}_4$  and  $\text{Co}_x\text{Fe}_{3-x}\text{O}_4$  nano-particles reveals the blue shift in absorption edge which is the confirmation of the formation of nano-particles [30].

The band gap of the samples is evaluated from the Tauc relation[31]:

$$(\alpha h\nu)^n = A(h\nu - E_g)^n \quad (8)$$

where  $E_g$  is the optical band gap energy and  $h$  is the planks constant ( $6.62 \times 10^{-34}$ ). The value of  $n$  for direct, indirect, allowed, and forbidden transitions is, 2, 1/2, and 3/2, respectively. The optical band gap energy of all the samples is estimated by extrapolating a straight line on  $x$ -axis which cuts the axis at some point; that point indicates the value of the optical band gap energy. The graph of  $E_g$  for all the samples is plotted in Fig. 13a, b, respectively. It is revealed that when the concentration of nickel and cobalt increases, the optical band gap energy increases. This may be due to the decrease in particle size, as shown in Fig. 14. When the crystallite size reaches the nano-scale where every element is made up of only a finite number of atoms, the electron hole pairs become very close together that the columbic force is no longer neglected and gives the overall higher kinetic energy. Hence, the larger band gap means that a large energy is required to excite an electron from valance to conduction band [32–35]. Optical band gap may also be increased because when the particle size decreases, the number of atoms becomes finite, the energy levels or overlapping orbitals decrease, and the width of the band starts to narrow. This narrowing of the band results in an increase in the optical band gap. The values of the optical band gap energy of all the samples are tabulated in Table 6.

### 4 Conclusion

$\text{Ni}_x\text{Fe}_{3-x}\text{O}_4$  and  $\text{Co}_x\text{Fe}_{3-x}\text{O}_4$  nano-particles with  $x = 0, 0.05, 0.1,$  and  $0.15$  have been prepared by co-precipitation method. The structural characterization displays that all the samples are composed of highly crystalline single-phase inverse spinel structure. FTIR analysis confirms the single phase with the major band at  $887 \text{ cm}^{-1}$ , which is due to the stretching vibrations of metal-oxide bond. SEM analysis revealed that the particles are spherical in shape. Thermal analysis shows that stability increases with the increasing Ni and Co concentrations in magnetite nano-particles. The magnetic measurement enlightens that the coercivity and anisotropy highly increase with cobalt doping in magnetite nano-particles as compared with nickel-doped magnetite nano-particles. This result has a great interest for magnetic fluid hyperthermia application. UV-visible analysis indicates the blue shift in the absorption edge of both nickel- and cobalt-doped magnetite nano-particles which also confirms the formation of nano-particles.

### References

1. Coker, V.S., Bennett, J.A., Telling, N.D., Henkel, T., Charnock, J.M., Van Der Laan, G., Patrick, R.A., Pearce, C.I., Cutting, R.S., Shannon, I.J.: Microbial engineering of nanoheterostructures: biological synthesis of a magnetically recoverable palladium nanocatalyst. *ACS Nano* **4**, 2577–2584 (2010)
2. Polshettiwar, V., Luque, R., Fihri, A., Zhu, H., Bouhrara, M., Basset, J.M.: Magnetically recoverable nanocatalysts. *Chem. Rev.* **111**, 3036–3075 (2011)
3. Alexiou, C., Arnold, W., Klein, R.J., Parak, F.G., Hulin, P., Bergemann, C., Erhardt, W., Wagenpfeil, S., Luebbe, A.S.: Locoregional cancer treatment with magnetic drug targeting. *Cancer Res.* **60**, 6641–6648 (2000)
4. Zeng, H., Black, C.T., Sandstrom, R.L., Rice, P.M., Murray, C.B., Sun, S.: Magnetotransport of magnetite nanoparticle arrays. *Phys. Rev. B* **73**, 020402 (2006)
5. Johannsen, M., Gneveckow, U., Eckelt, L., Feussner, A., Waldöfner, N., Scholz, R., Deger, S., Wust, P., Loening, S.A., Jordan, A.: Clinical hyperthermia of prostate cancer using magnetic nano-particles: Pof a new interstitial technique. *Int. J. Hyperthermia* **21**, 637–647 (2005)
6. Johannsen, M., Gneveckow, U., Thiesen, B., Taymoorian, K., Cho, C.H., Waldöfner, N., Scholz, R., Jordan, A., Loening, S.A.,

- Wust, P.: Thermotherapy of prostate cancer using magnetic nanoparticles: feasibility, imaging, and three-dimensional temperature distribution. *Eur. Urol.* **52**, 1653–1662 (2007)
7. Goya, G.F., Grazu, V., Ibarra, M.R.: Magnetic nano-particles for cancer therapy. *Curr. Nanosci.* **4**, 1–16 (2008)
  8. Fortin, J.P., Wilhelm, C., Servais, J., Ménager, C., Bacri, J.C., Gazeau, F.: Size-sorted anionic iron oxide nanomagnets as colloidal mediators for magnetic hyperthermia. *J. Am. Chem. Soc.* **129**, 2628–2635 (2007)
  9. Sorescu, M., Grabias, A., Tarabasanu-Mihaila, D., Diamandescu, L.: Influence of cobalt and nickel substitutions on populations, hyperfine fields, and hysteresis phenomenon in magnetite. *J. Appl. Phys.* **91**, 8135–8137 (2002)
  10. Philip, J., Laskar, J.M.: Optical properties and applications of ferrofluids—a review. *J. Nanofluids* **1**, 3–20 (2012)
  11. Staniland, S., Williams, W., Telling, N., Van Der Laan, G., Harrison, A., Ward, B.: Controlled cobalt doping of magnetosomes in vivo. *Nat. Nanotechnol.* **3**, 158–162 (2008)
  12. Stookey, L.L.: Ferrozine—a new spectrophotometric reagent for iron. *Anal. Chem.* **42**, 779–781 (1970)
  13. Niu, Z.P., Wang, Y., Li, F.S.: Magnetic properties of nanocrystalline Co–Ni ferrite. *J. Mater. Sci.* **41**, 5726–5730 (2006)
  14. Olsson, R.T., Salazar-Alvarez, G., Hedenqvist, M.S., Gedde, U.W., Lindberg, F., Savage, S.J.: Controlled synthesis of near-stoichiometric cobalt ferrite nano-particles. *Chem. Mater.* **17**, 5109–5118 (2005)
  15. Jacintho, G.V., Brolo, A.G., Corio, P., Suarez, P.A., Rubim, J.C.: Structural investigation of  $MFe_2O_4$  ( $M=Fe, Co$ ) magnetic fluids. *J. Phys. Chem. C* **113**, 7684–7691 (2009)
  16. Melo, T.F.O., Da Silva, S.W., Soler, M.A.G., Lima, E.C.D., Morais, P.C.: Investigation of surface passivation process on magnetic nano-particles by Raman spectroscopy. *Surf. Sci.* **600**, 3642–3645 (2006)
  17. Wang, X., Zhuang, J., Peng, Q., Li, Y.: A general strategy for nanocrystal synthesis. *Nature* **437**, 121–124 (2005)
  18. Sun, S., Zeng, H., Robinson, D.B., Raoux, S., Rice, P.M., Wang, S.X., Li, G.: Monodisperse  $MFe_2O_4$  ( $M=Fe, Co, Mn$ ) nanoparticles. *J. Am. Chem. Soc.* **126**, 273–279 (2004)
  19. Jana, N.R., Chen, Y., Peng, X.: Size- and shape-controlled magnetic (Cr, Mn, Fe, Co, Ni) oxide nanocrystals via a simple and general approach. *Chem. Mater.* **16**, 3931–3935 (2004)
  20. Rani, S., Varma, G.D.: Superparamagnetism and metamagnetic transition in  $Fe_3O_4$  nano-particles synthesized via co-precipitation method at different pH. *Phys. B: Cond. Matter* (2015)
  21. Shi, D. (ed.): High-temperature superconducting materials science and engineering. New concepts and technology. Pergamon, Oxford (2015)
  22. Larumbe, S., Gomez-Polo, C., Pérez-Landazábal, J.I., Garcia-Prieto, A., Alonso, J., Fdez-Gubieda, M.L., Cordero, D., Gómez, J.: Ni doped  $Fe_3O_4$  magnetic nano-particles. *J. Nanosci. Nanotechnol.* **12**, 2652–2660 (2012)
  23. Byrne, J.M., Coker, V.S., Moise, S., Wincott, P.L., Vaughan, D.J., Tuna, F., Arenholz, E., van der Laan, G., Patrick, R.A.D., Lloyd, J.R., Telling, N.D.: Controlled cobalt doping in biogenic magnetite nano-particles. *J. R. Soc. Interface.* **10**, 20130134 (2013)
  24. Priyadharsini, P., Pradeep, A., Rao, P.S., Chandrasekaran, G.: Structural, spectroscopic and magnetic study of nanocrystalline Ni–Zn ferrites. *Mater. Chem. Phys.* **116**, 207–213 (2009)
  25. Umare, S.S., Ningthoujam, R.S., Sharma, S.J., Shrivastava, S., Kurian, S., Gajbhiye, N.S.: Mössbauer and magnetic studies on nanocrystalline  $NiFe_2O_4$  particles prepared by ethylene glycol route. *Hyp. Interact.* **184**, 235–243 (2008)
  26. Tuo, Y., Liu, G., Dong, B., Zhou, J., Wang, A., Wang, J., Jin, R., Lv, H., Dou, Z., Huang, W.: Microbial synthesis of Pd/ $Fe_3O_4$ , Au/ $Fe_3O_4$  and PdAu/ $Fe_3O_4$  nanocomposites for catalytic reduction of nitroaromatic compounds. *Sci. Rep.*, 5 (2015)
  27. Pati, S.S., Philip, J.: A facile approach to enhance the high temperature stability of magnetite nano-particles with improved magnetic property. *J. Appl. Phys.* **113**, 044314 (2013)
  28. Manikandan, A., Vijaya, J.J., Mary, J.A., Kennedy, L.J., Dinesh, A.: Structural, optical and magnetic properties of  $Fe_3O_4$  nanoparticles prepared by a facile microwave combustion method. *J. Ind. Eng. Chem.* **20**, 2077–2085 (2014)
  29. Hu, L., De Montferrand, C., Lalatonne, Y., Motte, L., Brioude, A.: Effect of cobalt doping concentration on the crystalline structure and magnetic properties of monodisperse  $Co_xFe_{3-x}O_4$  nanoparticles within nonpolar and aqueous solvents. *J. Phys. Chem. C* **116**, 4349–4355 (2012)
  30. Jun, Y.W., Huh, Y.M.: Nanoscale size effect of magnetic nanocrystals and their utilization for cancer diagnosis via magnetic resonance imaging. *J. Amer. Chem. Soc.* **16**, 5743 (2005)
  31. Patange, S.M., Shirsath, S.E., Jadhav, S.S., Jadhav, K.M.: Cation distribution study of nanocrystalline  $NiFe_{2-x}Cr_xO_4$  ferrite by XRD, magnetization and Mössbauer spectroscopy. *Phys. Status Solidi (A)* **209**, 347–352 (2012)
  32. O’Leary, S.K., Lim, P.K.: On determining the optical gap associated with an amorphous semiconductor: a generalization of the Tauc model. *Solid State Commun.* **104**, 17–21 (1997)
  33. Mallick, P., Dash, B.N.: X-ray diffraction and UV-visible characterizations of  $-Fe_2O_3$  nano-particles annealed at different temperature. *Nanosci. Nanotechnol.* **3**, 130–134 (2013)
  34. El Ghandoor, H., Zidan, H.M., Khalil, M.M., Ismail, M.I.M.: Synthesis and some physical properties of magnetite ( $Fe_3O_4$ ) nano-particles. *Int. J. Electrochem. Sci.* **7**, 5734–5745 (2012)
  35. Sato, N.: *Electrochemistry at Metal and Semiconductor Electrodes*. Elsevier Science (1998)